

Magnetic response and antiferromagnetic correlations in strained kagome ribbonsR. F. P. Costa ¹, E. Vernek ^{1,2} and S. E. Ulloa ²¹*Instituto de Física, Universidade Federal de Uberlândia, Uberlândia, Minas Gerais 38400-902, Brazil*²*Department of Physics and Astronomy, and Nanoscale & Quantum Phenomena Institute, Ohio University, Athens, Ohio 45701-2979, USA*

(Received 6 June 2024; accepted 19 August 2024; published 3 September 2024)

We study the physics of the strong-coupling Hubbard model in a kagome lattice ribbon under mechanical tension and half filling. It is known that in the absence of strain, the lattice symmetry of the system and strong electronic interactions induce magnetic frustration. As uniaxial strain is applied, the ribbon exhibits various configurations with energy oscillations that depend on the direction of the strain axis. The ground states are obtained by density-matrix renormalization-group calculations. We find that the system is characterized by strong antiferromagnetic bonds distributed throughout the lattice in directions and patterns that depend on the strain directions and may coexist with easily polarizable sites that are only weakly correlated to their neighbors. We identify frustration and correlation measures that follow the strain and interaction dependence of the system well. These results illustrate that strain-dependent magnetic susceptibility could be explored experimentally to help probe the role of symmetry and interactions in these systems.

DOI: [10.1103/PhysRevB.110.115101](https://doi.org/10.1103/PhysRevB.110.115101)**I. INTRODUCTION**

The quantum spin liquid is an exotic and fascinating phase of matter [1–3]. Proposed by Anderson in [4], he suggested that such a phase could emerge as the ground state of a spin-1/2 antiferromagnet on geometrically frustrated triangular lattices [5]. However, after years of debate on whether a quantum spin-liquid (QSL) phase would emerge in a triangular antiferromagnet, detailed studies suggest this is not the case (see [1] and references therein). Indeed, the search for the realization of this elusive phase of matter has elicited great effort from the scientific community over the years [6–10].

In this context, the triangular motives present in kagome materials have attracted much attention in recent years [11]. Their unique crystal structure, consisting of corner-shared triangles arranged around a honeycomb structure, induces high geometrical frustration, offering thus the tantalizing possibility of stabilizing a QSL ground state [12–14]. Although magnetic insulating kagome lattices have been investigated for a long time [15], the interest in their electronic and magnetic properties has motivated a reexamination in the context of QSL phases. Theoretical studies on kagome lattices have explored interesting physical phenomena, including magnetic [16–19] and electronic [20–24] properties, QSL phases [14,25,26], and unconventional superconductivity [27–32]. Several materials have also been investigated experimentally, prominently including FeSn [33,34], CoSn [35], MnSn [36], and the rich class of materials AV_3Sb_5 with $A = K, Rb, Cs$ [37] and RV_6Sn_6 with $R = Gd, Ho, Y$ [38,39].

Different phases have been predicted theoretically in frustrated kagome lattices using antiferromagnetic Heisenberg and/or Hubbard models [40]. While the former accounts strictly for the spin degrees of freedom in the system, the latter also accounts for charge fluctuations and can then describe a wider range of phenomena. Schnyder *et al.* [17] showed that

different ground states could be obtained by controlling the spatial anisotropy of antiferromagnetic Heisenberg couplings on a kagome lattice, resulting in spiral phases and possible noncoplanar order. More recently, Nayga and Vojta [41] have also shown that the ground state of a kagome magnet with classical spins can be controlled by applied mechanical distortion of the lattice, including the finding that triaxial strain results in a noncoplanar spin-liquid phase. These studies point out that the magnetic properties of kagome systems are very sensitive to changes in the geometric frustration of the lattice. The reduction in symmetry would then be expected to strongly affect systems that incorporate charge fluctuations, such as those present in kagome metals. The Hubbard model provides a natural description, as the relative hoppings can be seen as effective control parameters that allow one to address the important question of how strain modifies the ground-state properties. Sun and Zhu [42] have shown recently that by controlling the Coulomb repulsion in a Hubbard model of a kagome ribbon it is possible to drive the system across multiple quantum phase transitions. This includes a strongly interacting regime where the ground state is effectively governed by an antiferromagnetic Heisenberg model and displays QSL characteristics. For weaker interaction, these authors saw evidence of different correlated phases in this geometrically frustrated system. We are interested in exploring the role that strain plays in the behavior of kagome systems as interactions change their response from the metallic to the insulating regime. The question we want to explore is how strain modifies possible frustrated ground states in the different regimes with varying correlations and charge fluctuations.

In this work we investigate the effect of a uniaxial uniform strain in a kagome nanoribbon. A schematic representation of the system is depicted in Fig. 1. Adopting a single-band Hubbard model, the effective role of strain is to modify the hopping matrix elements between electronic orbitals localized

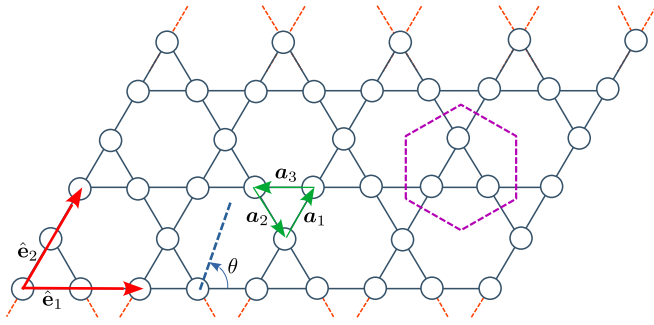


FIG. 1. Schematic representation of the kagome nanoribbon corresponding to $L_x = 4$ unit cells in the x direction and $L_y = 3$ unit cells in the \hat{e}_2 direction. Circles represent the atomic sites of a tight-binding model, while solid lines correspond to nearest-neighbor hopping matrix elements. Red dashed lines at the top and bottom indicate periodic boundaries, in which case the ribbon folds into what will be referred to as the long cylinder geometry. Directions \hat{e}_1 and \hat{e}_2 span the unit cell, while the \mathbf{a}_j ($j = 1, 2, 3$) represent the nearest-neighbor vectors. The angle θ defines the direction of applied strain with respect to \hat{e}_1 . The dashed magenta hexagon contains a minimal unit cell and associated bonds used in the text.

at the lattice sites. This generally results in anisotropic couplings along the three lattice vectors, thus reducing geometric frustration in the system. Furthermore, varying the Coulomb repulsion allows glancing at how magnetic properties of the metallic and insulating ground states differ, thereby highlighting the relevance of charge fluctuations.

By performing density-matrix renormalization-group (DMRG) calculations within a tensor networks platform [43,44], we compute the ground-state properties of the system, including the spatial distribution of spin-spin correlations and the local magnetization upon application of weak magnetic fields. Our results show that the anisotropy produced by the applied strain induces the formation of Néel lines of strongly antiferromagnetically correlated bonds arranged on different patterns and along different lattice directions, depending on the strain orientation. This behavior can be understood as arising from the suppression of the geometrical frustration in the system. Interestingly, we also find that scattered among the well-defined Néel lines with antiferromagnetic correlations, sites exist that are only weakly coupled to their neighbors. These interstitial sites are thus easily polarizable by weak external magnetic fields, while the Néel lines remain in their antiferromagnetic coupled structure. The pattern of Néel bonds and spatial distribution of polarizable sites depend critically on strain orientation and becomes more pronounced for larger values of Coulomb interaction as the system approaches the kagome antiferromagnet regime. To better characterize the response to strain, we introduce two intuitive quantities: a geometric indicator to quantify the structural frustration in the system and another that measures how local spin correlations reflect the degree of frustration in the ground state. These measures are good predictors of the different spin correlation profiles seen in the system as the strain and interaction change.

The remainder of this paper is organized as follows. In Sec. II we introduce the model and methods to study the

kagome lattice. In Sec. III we present and discuss our main findings. A summary and prospects for future work are presented in Sec. IV.

II. MODEL AND NUMERICAL METHODS

We consider a kagome lattice ribbon (see Fig. 1) described by a tight-binding Hubbard Hamiltonian as

$$H = \varepsilon_0 \sum_{j,\sigma} n_{j\sigma} - \sum_{\langle i,j \rangle} t_{ij} c_{i\sigma}^\dagger c_{j\sigma} + \sum_j (U n_{j\uparrow} n_{j\downarrow} + V_z S_j^z), \quad (1)$$

where $c_{j\sigma}^\dagger$ ($c_{j\sigma}$) creates (annihilates) an electron with energy ε_0 and spin σ at site j , $n_{j\sigma} = c_{j\sigma}^\dagger c_{j\sigma}$ is the number operator, $S_j^z = \hbar(n_{j\uparrow} - n_{j\downarrow})/2$ is the local spin z component, U represents the on-site Coulomb repulsion, and $V_z = g\mu_B B$ is the Zeeman energy due to a magnetic field B in the z direction. As defined in Appendix A, hopping matrix elements between nearest-neighbor sites (denoted by $\langle i, j \rangle$) are modified by the presence of a spatially homogeneous uniaxial strain in the ribbon as

$$t_{ij} \equiv t_\alpha(\theta) = t \exp[-\beta[\|\mathbf{a}'_\alpha(\theta)\| - 1]], \quad (2)$$

where β is the material-dependent Grüneisen parameter (approximately equal to 3 [45]), $\mathbf{a}'_\alpha = (\mathbf{I} + \bar{\epsilon})\mathbf{a}_\alpha$ are the strained vectors, and $\mathbf{a}_1 = \frac{1}{2}(1, \sqrt{3})$, $\mathbf{a}_2 = \frac{1}{2}(1, -\sqrt{3})$, and $\mathbf{a}_3 = -(\mathbf{a}_1 + \mathbf{a}_2) = (-1, 0)$ define the unstrained vectors (see Fig. 1), and set the nearest-neighbor separation as the unit length. The strain tensor is [24]

$$\bar{\epsilon} = \epsilon \begin{bmatrix} \cos^2 \theta - \nu \sin^2 \theta & (1 + \nu) \sin \theta \cos \theta \\ (1 + \nu) \sin \theta \cos \theta & \sin^2 \theta - \nu \cos^2 \theta \end{bmatrix}, \quad (3)$$

where ϵ is the strain strength, ν the material's Poisson ratio, and θ the direction of applied strain, as indicated in Fig. 1.

We are interested in the low-energy physics of the system, so our analysis involves mainly the ground state and a few excited ones, as needed. We employ the DMRG approach implemented within the ITENSOR library [43,44], a matrix product state platform suitable for obtaining many relevant physical quantities in quantum many-body Hamiltonians. We obtain associated physical quantities characteristic of the system, such as local magnetizations $M_j^y = \langle S_j^y \rangle$ and spin-spin correlations $C_{ij} = \langle \mathbf{S}_i \cdot \mathbf{S}_j \rangle - \langle \mathbf{S}_i \rangle \cdot \langle \mathbf{S}_j \rangle$, where \mathbf{S}_j is the spin operator on a given lattice site j and the terms in angular brackets represent the expectation values in the low-energy manifold. As defined, C_{ij} gives the intrinsic many-body correlations in the presence of an applied magnetic field by removing the trivial contribution induced by the polarizing field. In the absence of field, $M_j^y = 0$ for all ν , so $C_{ij} = \langle \mathbf{S}_i \cdot \mathbf{S}_j \rangle$ reduces to the usual expression. For visualization, it is useful to define the spatial link correlation as

$$C_{\text{link}}(x, y) = \sum_{i,j} C_{ij} e^{-d_{ij}(x,y)/b}, \quad (4)$$

where $d_{ij}(x, y)$ is the distance between any point on the xy plane and the segment that connects the lattice sites i and j , while b controls the sharpness of the link structure.

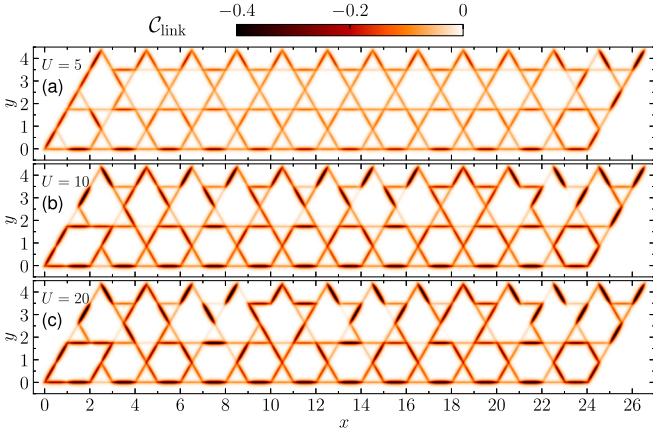


FIG. 2. Link correlations $\mathcal{C}_{\text{link}}$ in the absence of strain ($\epsilon = 0$) for (a) $U = 5$, (b) $U = 10$, and (c) $U = 20$. Darker links represent stronger antiferromagnetic alignments, clearly enhanced in (c). The uniform link distribution in (a) becomes more inhomogeneous for increasing U . Apart from strong links along the edges of this flat ribbon, there appears to be no overall order of the antiferromagnetic bonds in (c).

III. NUMERICAL RESULTS

We set $t = 1$ as the energy unit and $\hbar = 1$ hereafter, and ensure that the system is in the half-filling regime by setting $\epsilon_0 = -U/2$. We explore values of U from $U = 5$ to 20, corresponding to different phases of the system. For large values of U , the system is well described by an antiferromagnetic Heisenberg model [42]. The number of sites in the kagome nanoribbon increases rapidly with L_x and L_y , $N = L_y(3L_x + 2)$; we focus our analysis on a system with $L_x = 12$ and $L_y = 3$. Whenever the ribbon is folded along the \hat{e}_2 direction into a cylinder, with sites periodically coupled as indicated by red dashed lines in Fig. 1, we call such an arrangement the long cylinder geometry (LCG), which corresponds to the YC6 cylinder in Ref. [14]. For completely open boundaries, however, the configuration will be referred to as the flat ribbon geometry (FRG). We have allowed DMRG link dimension up to 5000, resulting in truncation errors typically less than 10^{-6} .

A. Unstrained vs strained regimes

We first look at the spin-spin correlations in the system for a strain-free FRG lattice, $\epsilon = 0$. As defined above, we use $\mathcal{C}_{\text{link}}$ to provide a convenient visualization of the correlations. Figure 2 shows a heat map of $\mathcal{C}_{\text{link}}$ for different Hubbard interaction values, placing the system into different phases: $U = 5$ [Fig. 2(a)], the metallic phase; $U = 10$ [Fig. 2(b)]; and $U = 20$ [Fig. 2(c)], the quantum-spin-liquid/kagome antiferromagnetic phase [42]. As the color bar shows, darker links correspond to stronger antiferromagnetic pairs. For small U , the correlation links are not as strong and are homogeneously distributed, as the weak interactions in this metallic regime would suggest. Despite the homogeneous distribution of hopping terms in the Hamiltonian, we notice some differences, likely due to edge effects on the ribbon. For larger U , the antiferromagnetic correlations appear stronger (darker links) and not as homogeneously distributed as the system approaches

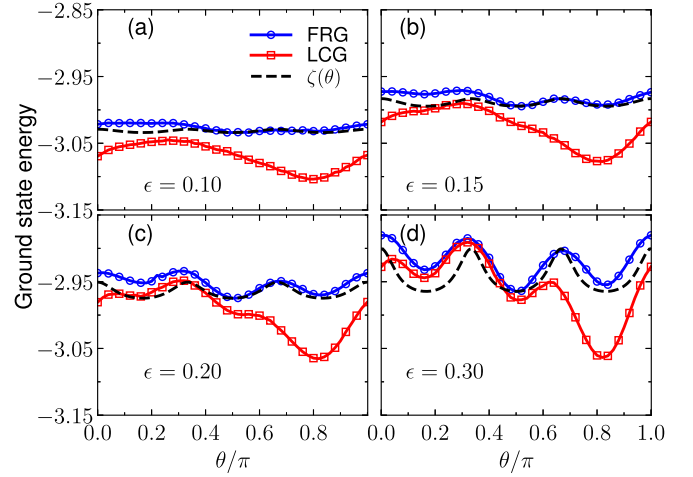


FIG. 3. (a) Ground-state energy per site E_0/N as a function of strain direction θ for (a) $\epsilon = 0.10$, (b) $\epsilon = 0.15$, (c) $\epsilon = 0.20$, and (d) $\epsilon = 0.30$. Blue and red curves correspond to flat ribbon geometry and long cylinder geometry, respectively. The black dashed line shows $\zeta(\theta)$ defined in Eq. (5) and scaled as per [46]. In all panels $U = 5$, i.e., the metallic regime for the unstrained system.

the Heisenberg antiferromagnetic regime. In an infinite system, the spin-dominated ground state is expected to have high frustration without strain. A spin-liquid phase may even emerge, with not yet fully understood characteristics [14,42]. We aim to study the role that strain may play in modifying the frustration otherwise present in the system. We will contrast Fig. 2 with the link correlation in the presence of strain to expose some of its effects on the ground state. All link correlations plotted in this paper are for FRG.

We now analyze the effect of strain on the link-correlation pattern over the ribbon. Because the effect of strain on the correlations depends on the angle θ , it is instructive to first analyze how the ground-state energy E_0 changes with θ . Figure 3 shows $E_0(\theta)$ vs θ for $U = 5$ and increasing strain values. Blue circles and red squares correspond to FRG and LCG, respectively. In all cases, E_0 exhibits an oscillatory behavior with maxima and minima as θ varies from 0 to π , as well as an overall increasing value for larger strains. The oscillations with strain direction are better defined for $\epsilon = 0.30$ [Fig. 3(d)] but are already visible for $\epsilon = 0.15$ [see Fig. 3(b)]. The minima occur for $\theta \simeq \pi/6, \pi/2, \text{ and } 5\pi/6$, which correspond to strain applied orthogonal to one of the lattice vectors \mathbf{a}_j . In contrast, the E_0 maxima are observed around $\theta = 0, \pi/3, \text{ and } 2\pi/3$, for which the strain direction lies along one of the lattice vectors. The general behavior of E_0 increasing with ϵ can be seen to be associated with the suppression of antiferromagnetic correlations, which contribute to lowering the energy of the system. This is consistent with the fact that for LCG E_0 is lower, as additional singletlike correlations appear across the edges. We also notice that $E_0(\theta)$ is not fully symmetric around $\theta = \pi/2$, a direct consequence of the slanted geometry that defines the ends of the ribbon. Such asymmetry is even more pronounced for LCG, as seen in the red curves of Fig. 3. This feature becomes clear once one realizes that, for LCG, the configurations in Figs. 4(e) and 4(f) loop \mathbf{a}_1 lines onto themselves (see Fig. 1), in great contrast to

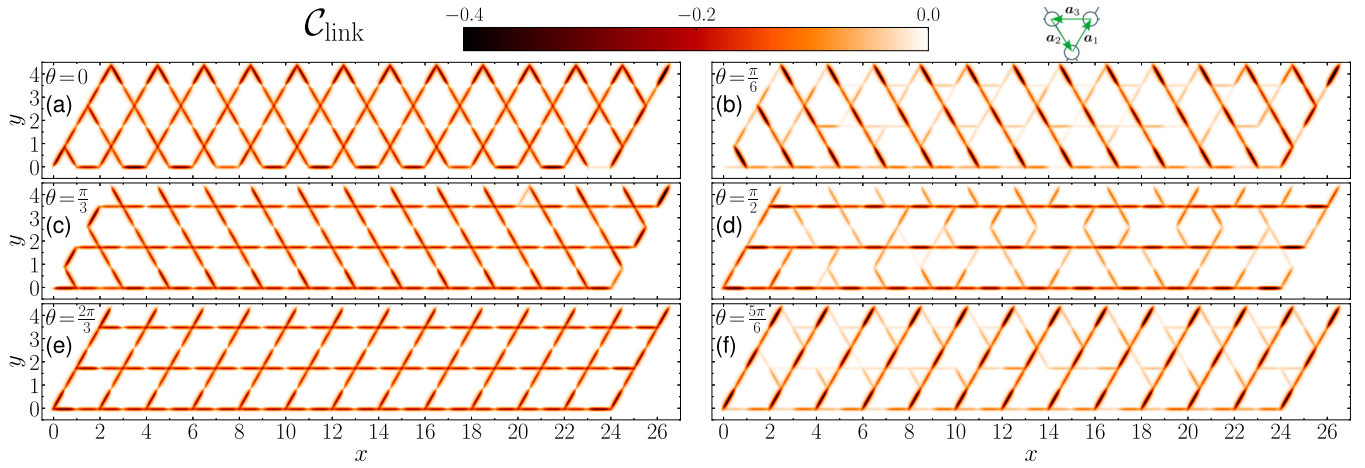


FIG. 4. Link correlations for $\epsilon = 0.30$ and different strain orientations (a) $\theta = 0$, (b) $\theta = \pi/6$, (c) $\theta = \pi/3$, (d) $\theta = \pi/2$, (e) $\theta = 2\pi/3$, and (f) $\theta = 5\pi/6$. The left (right) column corresponds to maxima (minima) in $E_0(\theta)$ of Fig. 3. (a), (c), and (e) For energy maxima, links with antiferromagnetic correlations form 2D oblique Lieb-like lattices. (b), (d), and (f) For energy minima, links form 1D-like arrays with stronger (darker) antiferromagnetic correlations. In all panels $U = 5$. The inset above (b) shows nearest-neighbor vectors to help identify the link orientations.

what happens with the remaining ones; for example, \mathbf{a}_2 lines are alternately coupled with one another in Figs. 4(b) and 4(c).

To gain more intuition on the behavior of E_0 vs θ shown in Fig. 3, we analyze the nature of the maxima and minima of $E_0(\theta)$. Intuitively, one would expect the system to be more frustrated if all couplings were equal. It is thus reasonable to explore the distinct hoppings t_j along different lattice vectors \mathbf{a}_j , as the strain changes them according to Eq. (2). We quantify the isotropy of the couplings by analyzing their distribution, as a smaller dispersion in hopping constants favors frustration in the system's ground state. The simplest measure of dispersion of hoppings is given by the variance σ^2 . We introduce the inverse of σ^2 as a measure of the homogeneity of the couplings, defining a geometric frustration function as

$$\zeta(\theta) = \frac{1}{\sigma^2} = \frac{N_t(N_t - 1)}{\sum_{j=1}^{N_t} (t_j - \bar{t})^2} = \frac{6}{\sum_{j=1}^3 (t_j - \bar{t})^2}, \quad (5)$$

where $\bar{t} = (t_1 + t_2 + t_3)/3$ and $N_t = 3$ is the number of distinct hoppings in the kagome lattice. Note that Eq. (5) depends implicitly on θ through both t_j and \bar{t} .

This quantity can be scaled and compared with the ground-state energy $E_0(\theta)$ [46]. Figure 3 shows $\zeta(\theta)$ as a black dashed curve; evidently, the scaled function $\zeta(\theta)$ follows $E_0(\theta)$ quite well. As mentioned above, the results for LCG are more affected by end effects and the agreement is poorer. Nevertheless, the positions of maxima and minima predicted by $\zeta(\theta)$ agree quite nicely with $E_0(\theta)$ for both FRG and LCG configurations obtained via DMRG. These results suggest that the maxima of $E_0(\theta)$ are obtained whenever the geometric frustration in the system is higher, even for the case $U = 5$ (metallic regime when unstrained) shown in Fig. 3.

We now turn our attention to the effect of strain on the spin-spin correlations in the kagome ribbon. Figure 4 shows the heatmap of C_{link} for angles where E_0 and ζ have maxima, i.e., higher frustration $\theta = 0, \pi/3$, and $2\pi/3$ [Figs. 4(a), 4(c),

and 4(e)], or minima, i.e., lower frustration $\theta = \pi/6, \pi/2$, and $5\pi/6$ [Figs. 4(b), 4(d), and 4(f)]. We note that C_{link} exhibits a structure of connected oblique Lieb-like lattices [47] for strain directions where ζ is maximum [Figs. 4(a), 4(c), and 4(e)]. The links are homogeneous in strength/intensity throughout, with links stretched the most (those along θ) having nearly vanishing correlation strength. In contrast, for angles where E_0 is minimum [Figs. 4(b), 4(d), and 4(f)], the C_{link} distribution appears as quasi-independent one-dimensional (1D) chains of strong correlation links at angles orthogonal to strain direction θ .

These features in the overall link distribution are even more pronounced for larger values of the Coulomb interaction U , as charge fluctuations are suppressed and antiferromagnetic correlations enhanced overall. This is evident in Fig. 5, which shows link correlations for $U = 10$ [Figs. 5(a) and 5(b)] and $U = 20$ [Figs. 5(c) and 5(d)]. Figures 5(a) and 5(c) and Figs. 5(b) and 5(d) refer to $\theta = \pi/3$ and $\pi/6$, which compare with Figs. 4(c) and 4(b), respectively. Note that the Néel-like lines [Figs. 5(b) and 5(d)] and the oblique 2D lattice structures [Figs. 5(a) and 5(c)] are much more pronounced in this figure than in Fig. 4. We also note relatively little variation between $U = 10$ and 20.

While $\zeta(\theta)$ is a good indicator of θ values that most affect the ground-state energy E_0 , it does not directly quantify the spin frustration that may be present in the system. (Yet another indicator is discussed in Appendix B). A useful way to quantify the frustration content of the ground state is via the quantity

$$f_j^G = 1 - \frac{4}{J_j} \left| \sum_{(m,n) \in C_B^j} J_{mn} \langle S_m^z S_n^z \rangle \right|, \quad (6)$$

which accounts for the spin-spin correlations within a given unit cell of the kagome system. In this expression, $J_{mn} = 4t_{mn}^2/U$ represents the exchange coupling between neighbor

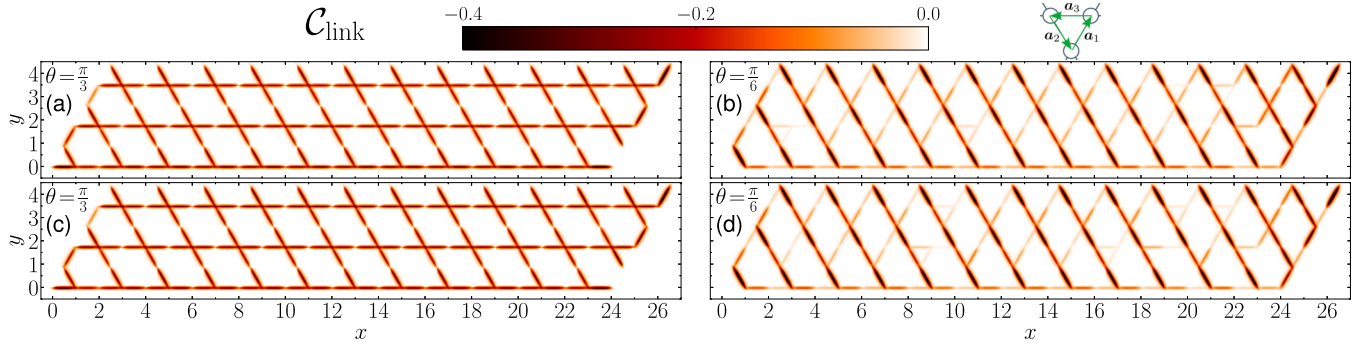


FIG. 5. Link correlations for $\epsilon = 0.30$ (a) and (c) along \mathbf{a}_1 [$\theta = \pi/3$, a maximum in $E_0(\theta)$] and (b) and (d) orthogonally to \mathbf{a}_2 [$\theta = \pi/6$, a minimum in $E_0(\theta)$] for (a) and (b) $U = 10$ and (c) and (d) $U = 20$. These configurations occur whenever strain is applied along \mathbf{a}_1 and orthogonally to \mathbf{a}_2 , in this order [see the inset above (b)]. Compared to Figs. 4(b) and 4(c), the correlations here are much more pronounced, with little difference between $U = 10$ and 20.

spins (m, n) within the unit cell considered, \mathbb{C}_B^j , and included in the sum. The unit cell used is shown by magenta dashed lines in Fig. 1. Finally, $\tilde{J}_j \equiv \sum_{(m,n) \in \mathbb{C}_B^j} J_{mn}$. In this definition, f_j^G accounts for the couplings (including their the sign) between each pair of spins in all unit cells. Notice that $f_j^G \rightarrow 1$ for uncorrelated cells, while $f_j^G \rightarrow 0$ for both fully ferro- and antiferromagnetic correlated links.

Figure 6 shows the average of this indicator over the entire system, $f^G(\theta)$, for three distinct values of U , over the range $0 < \theta < \pi/2$; apart from small end-effect asymmetry, similar results are obtained for $\pi/2 < \theta < \pi$. Notice that for large $U = 10$ and 20, where antiferromagnetic correlations are better defined in the system, f^G drops in value overall and exhibits well-pronounced maxima and minima that agree well with the corresponding behavior of $E_0(\theta)$ in Fig. 3. The nearly flat behavior of $f^G(\theta)$ for $U = 5$ is likely associated with charge fluctuations in the system, suppressing local moments in lattice sites for weak interactions. This indicator is then not as effective in providing a quantitative assessment in the weak-interaction regime, despite the clear impact of strain on the \mathbb{C}_{link} distribution.

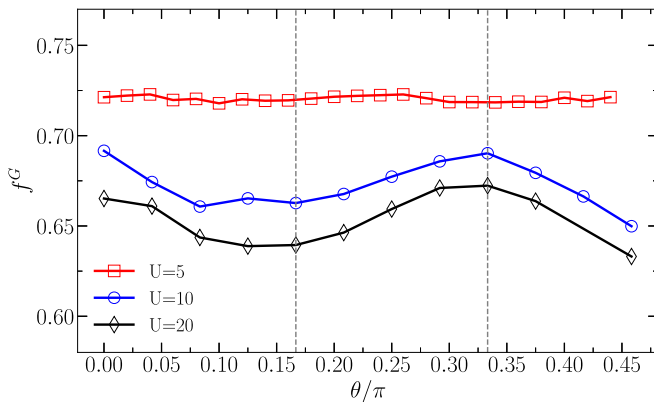


FIG. 6. Plot of $f^G(\theta)$ vs θ for $\epsilon = 0.30$ and $U = 5$ (red squares), $U = 10$ (blue circles), and $U = 20$ (black diamonds). Note that for larger values of U , the maxima and minima become more pronounced, as expected. Dashed lines indicate $\theta = \pi/6, \pi/3$ for the minimum and maximum in E_0 .

B. Coexistent magnetization and Néel structures

Let us go back to link correlations for the strained case and take a closer look at Fig. 4. Note that for angles where ζ or E_0 have a minimum [Figs. 4(b), 4(d), and 4(f)], the formation of 1D correlated lines conspire to leave the sites between lines only loosely coupled to their neighbors. This suggests the coexistence of antiferromagnetic links and paramagnetic sites in the lattice. One would further expect these two types of sites (free and correlated) would respond differently to an applied magnetic field. The (antiferromagnetically) correlated spins would require a larger field to be polarized, as the field should compete with the effective exchange interaction. On the other hand, the loose spins would align readily with the field.

To verify this reasoning, we apply a small magnetic field in the z direction to the entire system and analyze the behavior of the spatially resolved magnetization over the lattice. Figure 7 shows the local z magnetization $M_j^z = \langle S_j^z \rangle$ for the ground state in a small applied field $V_z = 0.05$ and for the same strain angles as in Fig. 4. Colored dots at each site of the lattice indicate whether that spin is polarized towards $+\hat{z}$ (red) or $-\hat{z}$ (blue) or unpolarized (white), as per the color scale. Let us analyze what is shown in Fig. 7. Starting with the case of $\theta = 0$ [Fig. 7(a)], we observe a pattern consisting of alternating positive/negative M_j^z for j on the line along the vectors \mathbf{a}_1 or \mathbf{a}_2 with all positive M_j^z along \mathbf{a}_3 . This pattern can be connected with Fig. 4(a) as follows: Since the weakest link correlations are seen there along \mathbf{a}_3 , the application of a magnetic field easily polarizes all spins parallel to the field for sites along \mathbf{a}_3 ; in contrast, sites along \mathbf{a}_1 and \mathbf{a}_2 align antiferromagnetically to those polarized by the field. The antiferromagnetic (AF) links remain intact because, for this weak field, it is still energetically favorable to form the Néel lines along with strong link correlations. Similar conclusions can be made for the cases of $\theta = \pi/3$ and $2\pi/3$, except that the weakest links in these cases lie along \mathbf{a}_1 and \mathbf{a}_2 , respectively. We emphasize that sites aligned with the field and lying along \mathbf{a}_3 in Fig. 7(a) are consistent with the formation of AF lines along \mathbf{a}_1 and \mathbf{a}_2 in Fig. 4(a) and that the AF many-body correlations are not suppressed for small fields, as one would expect.

Let us now look at Figs. 7(b), 7(d), and 7(f) for which the frustration ζ and E_0 have minima. The Néel lines with

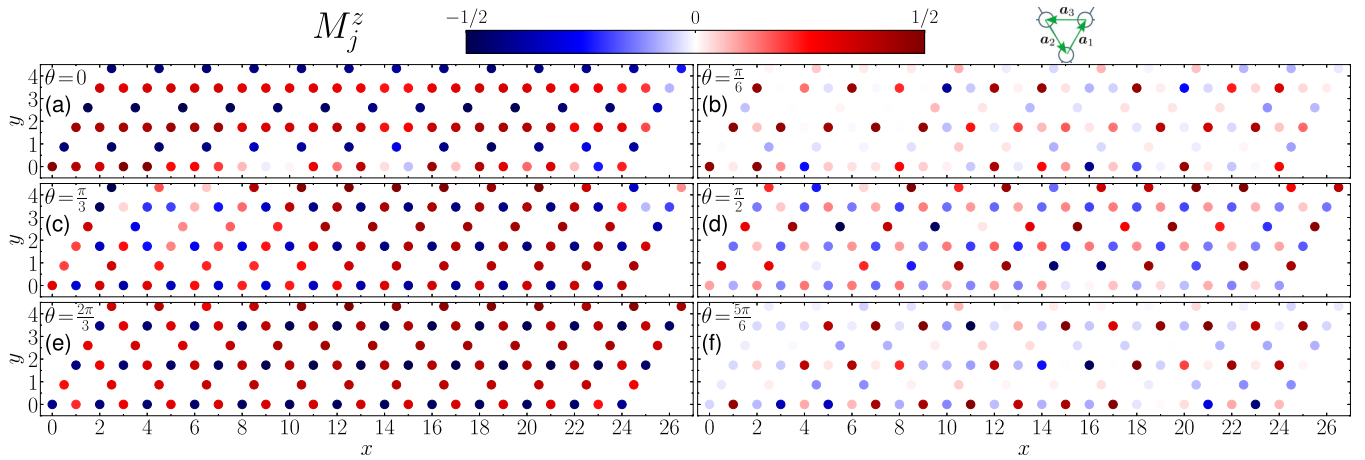


FIG. 7. Magnetization M_j^z for $V_z = 0.05$ and (a) $\theta = 0$, (b) $\theta = \pi/6$, (c) $\theta = \pi/3$, (d) $\theta = \pi/2$, (e) $\theta = 2\pi/3$, and (f) $\theta = 5\pi/6$. For all panels, we set $U = 5$ and $\epsilon = 0.30$. Faint dots in (b), (d), and (f) (where E_0 has minima in Fig. 3) feature sites belonging to Néel-like lines, while dark red dots correspond to loose sites readily polarized by the field. The inset above (b) helps identify, e.g., the red lines in (c) as being in the strain direction \mathbf{a}_1 .

strong link correlation of Fig. 4(b) (for $\theta = \pi/6$) lie parallel to the lattice vector \mathbf{a}_2 . This is manifested in the faint, nearly unpolarized sites along \mathbf{a}_2 in Fig. 7(b), suggesting that the Néel lines are not affected by the external field. Note also in Fig. 7(b) that the alternating polarization of sites is not as well pronounced as for the maximal E_0 cases. Most important, however, are the dark red sites between Néel lines which strongly polarize regardless of their neighbors and are scattered throughout the system. This is consistent with the idea that loosely connected sites exist over the lattice that respond efficiently to the applied field.

The coexistence of distinct magnetic structures, strongly correlated links, and easily polarizable loose sites is expected to be more pronounced for larger values of U . To test this, Fig. 8 shows M_j^z for $U = 10$ [Figs. 8(a) and 8(b)] and $U = 20$ [Figs. 8(c) and 8(d)] for the same magnetic field $V_z = 0.05$. Figures 8(a) and 8(c) and Figs. 8(b) and 8(d) correspond to $\theta = \pi/3$ and $\pi/6$, respectively, corresponding to the lattice strains in Fig. 5. We again observe in Figs. 8(a) and 8(c) that the weakly correlated sites along the θ direction \mathbf{a}_1 become easily polarized by the field, while the neighboring sites are/remain strongly AF correlated along \mathbf{a}_2 and \mathbf{a}_3 [as in

Fig. 7(c)]. Figures 8(b) and 8(d) show that the energy is minimized on alternating diagonal lines that weakly polarize in the field while coexisting with strongly polarized sites through the structure, similarly to Fig. 7(b).

Finally, one may wonder whether the applied magnetic field destroys the many-body spin correlations. We expect them to be robust along well-defined Néel lines. To confirm this, Fig. 9 shows the link correlations for systems as in Figs. 4(a) and 4(b) under an applied field. Comparing these two figures, it is clear that correlations along the strong links are indeed preserved for the applied field $V_z = 0.05$. Interestingly, correlations along the lower edge are more affected, likely due to their fewer neighbors. Notice again that the Néel lines are parallel to the lattice vector \mathbf{a}_2 in Figs. 9(b) and 4(b) as the sites in between adjacent lines are weakly correlated to their neighbors and are then strongly polarizable by the field, as seen in Fig. 7(b). These sites behave as a collection of paramagnetic (noninteracting) polarizable spins, while the sites belonging to Néel lines form a separate set of AF 1D chains. The coexistence of these two classes of sites and the dependence of their appearance and orientation with applied strain represent the main unexpected results of this work.

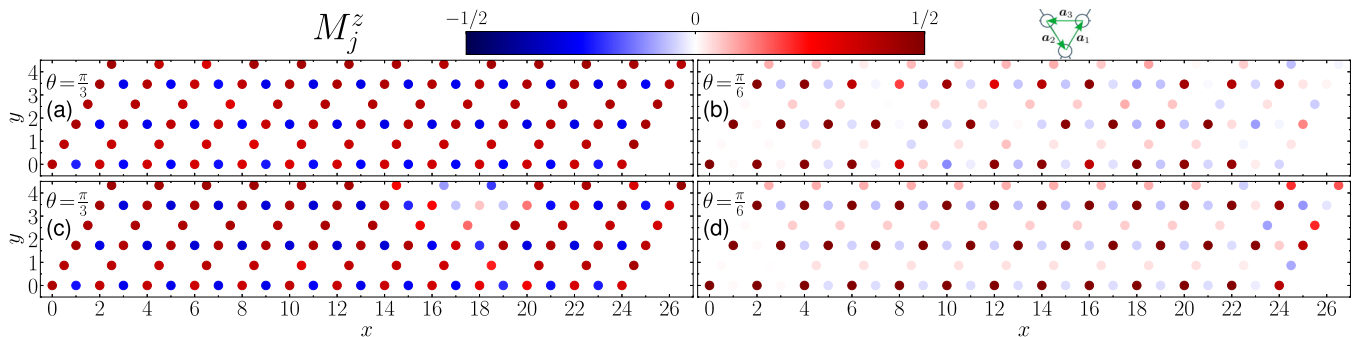


FIG. 8. Local magnetization M_j^z for $V_z = 0.05$ and strain applied along (a) and (c) $\theta = \pi/3$ and (b) and (d) $\theta = \pi/6$ for (a) and (b) $U = 10$ and (c) and (d) $U = 20$. As in Fig. 7, faint dots in (b) and (d) represent sites belonging to Néel AF lines, while dark red dots correspond to loose sites more easily polarized by the field. Notice how the most energetically favorable top left to bottom right red-then-blue pattern results along \mathbf{a}_2 -connected spins. For all panels, $\epsilon = 0.30$.

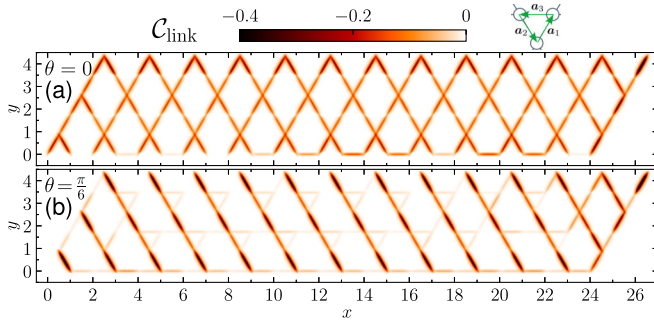


FIG. 9. Link correlations for $\epsilon = 0.30$ and $V_c = 0.05$, with (a) $\theta = 0$ and (b) $\theta = \pi/6$, corresponding to the maximum and minimum of the frustration quantifier shown in Fig. 3. In (a) all sites are connected with neighbors along Néel AF lines forming a 2D lattice. In (b) Néel lines are disconnected from each other, leaving many sites nearly fully uncorrelated. In both panels $U = 5$.

IV. CONCLUSION

We have studied a kagome nanoribbon using a Hubbard model to describe how anisotropies induced by uniaxial strain break the symmetry and affect the correlations due to electronic repulsion. We found that even for relatively weak interactions, the competing correlations and frustration develop coexisting systems of strongly antiferromagnetic correlations between neighboring sites and weakly connected sites that are easily polarizable in a magnetic field. The spatial distribution of the strong links and interspersed paramagnetic sites depends strongly on the orientation of the uniaxial strain and opens the possibility of exploring an experimentally tunable probe that can give rise to different correlated behavior in a given lattice. The need to consider charge fluctuations to define a function that quantifies correlations, especially for weak U values, and that complements f^G remains an interesting theoretical question. With the growing interest in metallic kagome materials displaying strongly correlated behavior, it may be possible to apply external strain fields and explore

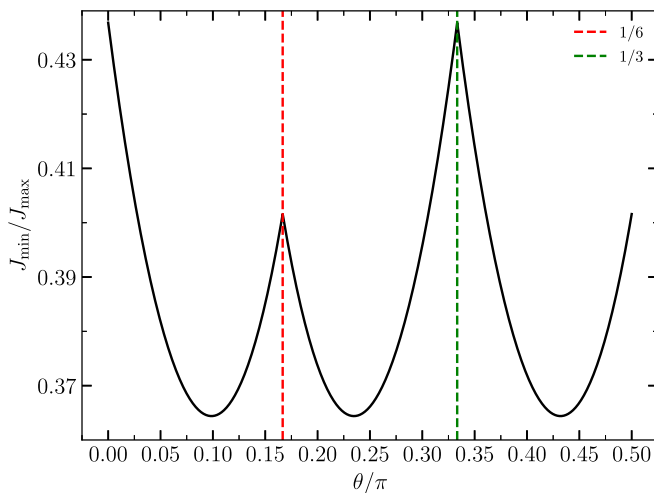


FIG. 10. Plot of $r(\theta)$ vs θ for $\epsilon = 0.30$. Note that this quantity is U independent. Dashed lines indicate $\theta = \pi/6, \pi/3$ for a minimum and maximum in E_0 .

some of the phenomena our models describe. It would be interesting, moreover, to explore how distinct Fermi levels and proximity to Van Hove singularities in different materials affect this behavior. As a final reflection, there might be a connection between our results and the spin Jahn-Teller effect. The idea that spontaneous distortions could play a role in kagome materials is appealing and deserves future investigation.

ACKNOWLEDGMENTS

E.V. acknowledges financial support from CNPq (Grant No. 311366/2021-0), FAPEMIG (Grant No. PPM-00631-17), and CAPES under the UFU-CAPES Print initiative. S.E.U. acknowledges support from the U.S. Department of Energy, Office of Basic Energy Sciences, Materials Science and Engineering Division.

APPENDIX A: STRAINED COUPLINGS

The deformed nearest-neighbor vectors are given by

$$\mathbf{a}'_j = (\mathbf{I} + \bar{\epsilon})\mathbf{a}_j, \quad (\text{A1})$$

with

$$\mathbf{a}_1 = \frac{a_0}{2}(1, \sqrt{3}), \quad \mathbf{a}_2 = \frac{a_0}{2}(1, -\sqrt{3}), \quad \mathbf{a}_3 = a_0(-1, 0),$$

and the strain tensor $\bar{\epsilon}$ is given by Eq. (3). We set the lattice constant $a_0 = 1$. Using trigonometric identities, we can readily write

$$\bar{\epsilon} = \frac{\epsilon}{2}[(1 - \nu)\mathbf{I} + (1 + \nu)\tilde{\mathbf{R}}(\theta)], \quad (\text{A2})$$

where

$$\tilde{\mathbf{R}}(\theta) = \begin{bmatrix} \cos(2\theta) & \sin(2\theta) \\ \sin(2\theta) & -\cos(2\theta) \end{bmatrix} = \tilde{\mathbf{R}}^T(\theta), \quad (\text{A3})$$

which is then an orthogonal symmetric tensor

$$\tilde{\mathbf{R}}(\theta)\tilde{\mathbf{R}}^T(\theta) = \tilde{\mathbf{R}}^T(\theta)\tilde{\mathbf{R}}(\theta) = [\tilde{\mathbf{R}}(\theta)]^2 = \mathbf{I}. \quad (\text{A4})$$

Now, by defining $\alpha_{\pm} \equiv (1 \pm \nu)/2$, we can recast Eq. (A1) as

$$\mathbf{a}'_j(\theta) = [(1 + \alpha_-)\mathbf{I} + \alpha_+\tilde{\mathbf{R}}(\theta)]\mathbf{a}_j. \quad (\text{A5})$$

The strained hopping terms to be calculated are given by

$$t_j(\theta) = t_j \exp\{-\beta[|\mathbf{a}'_j(\theta)| - 1]\}. \quad (\text{A6})$$

The strained vectors' moduli $|\mathbf{a}'_j(\theta)| = \sqrt{\mathbf{a}'_j(\theta) \cdot \mathbf{a}'_j(\theta)}$, and since $\tilde{\mathbf{R}}$ is both symmetric and orthogonal, we get

$$\begin{aligned} \mathbf{a}'_j(\theta) \cdot \mathbf{a}'_j(\theta) &= [\alpha_+^2 + (1 + \alpha_-)^2]\mathbf{a}_j \cdot \mathbf{a}_j + 2\alpha_+(1 + \alpha_-)\mathbf{a}_j \\ &\quad \cdot \tilde{\mathbf{a}}_j(\theta), \end{aligned} \quad (\text{A7})$$

where $\tilde{\mathbf{a}}_j(\theta) \equiv \tilde{\mathbf{R}}(\theta)\mathbf{a}_j$. Finally, using the traditional definition of antiferromagnetic energy scale $J_n = 4t_n^2/U$, we obtain

the effective strain-induced Heisenberg couplings

$$J_n(\theta) = J_n \exp \left\{ -2\beta \left[\left([\alpha_+^2 + (1 + \alpha_-)^2] + 2\alpha_+(1 + \alpha_-) \frac{1}{x_n^2 + y_n^2} [(x_n^2 - y_n^2) \cos(2\theta) + 2x_n y_n \sin(2\theta)] \right)^{1/2} - 1 \right] \right\}, \quad (\text{A8})$$

where $\mathbf{a}_j = (x_j, y_j)$.

APPENDIX B: COUPLING RATIOS

For each angle θ , we display the ratio $r(\theta) \equiv J_{\min}(\theta)/J_{\max}(\theta)$ between the smallest and largest couplings in Fig. 10. This is a nonanalytical function, with cusps located

at the stationary points in Fig. 3. Consistent with Eqs. (5) and (6), the plot reflects that $r(\theta)$ values closer to one indicate greater homogeneity of couplings, thus implying higher frustration, hence the peak at, e.g., $\theta = \pi/3$ being taller than the one at $\theta = \pi/6$. We conclude that $r(\theta)$ is a much coarser way to infer frustration and therefore not as useful an indicator as those discussed in the main text.

-
- [1] Y. Zhou, K. Kanoda, and T.-K. Ng, Quantum spin liquid states, *Rev. Mod. Phys.* **89**, 025003 (2017).
- [2] C. Broholm, R. J. Cava, S. A. Kivelson, D. G. Nocera, M. R. Norman, and T. Senthil, Quantum spin liquids, *Science* **367**, eaay0668 (2020).
- [3] S. Kivelson and S. Sondhi, 50 years of quantum spin liquids, *Nat. Rev. Phys.* **5**, 368 (2023).
- [4] P. Anderson, Resonating valence bonds: A new kind of insulator? *Mater. Res. Bull.* **8**, 153 (1973).
- [5] P. Fazekas and P. W. Anderson, On the ground state properties of the anisotropic triangular antiferromagnet, *Philos. Mag.* **30**, 423 (1974).
- [6] M. R. Norman, *Colloquium*: Herbertsmithite and the search for the quantum spin liquid, *Rev. Mod. Phys.* **88**, 041002 (2016).
- [7] A. Wietek, S. Capponi, and A. M. Läuchli, Quantum electrodynamics in 2 + 1 dimensions as the organizing principle of a triangular lattice antiferromagnet, *Phys. Rev. X* **14**, 021010 (2024).
- [8] O. Starykh, Viewing a quantum spin liquid through QED, *Physics* **17**, 63 (2024).
- [9] J. Wen, S.-L. Yu, S. Li, W. Yu, and J.-X. Li, Experimental identification of quantum spin liquids, *npj Quantum Mater.* **4**, 12 (2019).
- [10] T. Imai and Y. S. Lee, Do quantum spin liquids exist? *Phys. Today* **69** (8), 30 (2016).
- [11] Y. Wang, H. Wu, G. T. McCandless, J. Y. Chan, and M. N. Ali, Quantum states and intertwining phases in kagome materials, *Nat. Rev. Phys.* **5**, 635 (2023).
- [12] F. Mila, Low-energy sector of the $S = 1/2$ kagome antiferromagnet, *Phys. Rev. Lett.* **81**, 2356 (1998).
- [13] T. Yavors'kii, W. Apel, and H.-U. Everts, Heisenberg antiferromagnet with anisotropic exchange on the kagomé lattice: Description of the magnetic properties of volborthite, *Phys. Rev. B* **76**, 064430 (2007).
- [14] S. Yan, D. A. Huse, and S. R. White, Spin-liquid ground state of the $S = 1/2$ kagome Heisenberg antiferromagnet, *Science* **332**, 1173 (2011).
- [15] I. Syozi, Statistics of kagome lattice, *Prog. Theor. Phys.* **6**, 306 (1951).
- [16] A. B. Harris, C. Kallin, and A. J. Berlinsky, Possible Néel orderings of the kagomé antiferromagnet, *Phys. Rev. B* **45**, 2899 (1992).
- [17] A. P. Schnyder, O. A. Starykh, and L. Balents, Spatially anisotropic Heisenberg kagome antiferromagnet, *Phys. Rev. B* **78**, 174420 (2008).
- [18] H. C. Jiang, Z. Y. Weng, and D. N. Sheng, Density matrix renormalization group numerical study of the kagome antiferromagnet, *Phys. Rev. Lett.* **101**, 117203 (2008).
- [19] H. Nakano, T. Shimokawa, and T. Sakai, Collapse of ferrimagnetism in two-dimensional Heisenberg antiferromagnet due to frustration, *J. Phys. Soc. Jpn.* **80**, 033709 (2011).
- [20] S. Guertler, Kagome lattice Hubbard model at half filling, *Phys. Rev. B* **90**, 081105(R) (2014).
- [21] H.-M. Guo and M. Franz, Topological insulator on the kagome lattice, *Phys. Rev. B* **80**, 113102 (2009).
- [22] A. Bolens and N. Nagaosa, Topological states on the breathing kagome lattice, *Phys. Rev. B* **99**, 165141 (2019).
- [23] S. Okamoto, N. Mohanta, E. Dagotto, and D. N. Sheng, Topological flat bands in a kagome lattice multiorbital system, *Commun. Phys.* **5**, 198 (2022).
- [24] M. A. Mojarro and S. E. Ulloa, Strain-induced topological transitions and tilted Dirac cones in kagome lattices, *2D Mater.* **11**, 011001 (2024).
- [25] C. Peng, Y. Jiang, D. Sheng, and H. Jiang, Doping quantum spin liquids on the kagome lattice, *Adv. Quantum Technol.* **4**, 2000126 (2021).
- [26] H.-C. Jiang, T. Devereaux, and S. A. Kivelson, Holon Wigner crystal in a lightly doped kagome quantum spin liquid, *Phys. Rev. Lett.* **119**, 067002 (2017).
- [27] M. L. Kiesel, C. Platt, and R. Thomale, Unconventional Fermi surface instabilities in the kagome Hubbard model, *Phys. Rev. Lett.* **110**, 126405 (2013).
- [28] M. Kang, S. Fang, J.-K. Kim, B. R. Ortiz, S. H. Ryu, J. Kim, J. Yoo, G. Sangiovanni, D. Di Sante, B.-G. Park, C. Jozwiak, A. Bostwick, E. Rotenberg, E. Kaxiras, S. D. Wilson, J.-H. Park, and R. Comin, Twofold van Hove singularity and origin of charge order in topological kagome superconductor CsV₃Sb₅, *Nat. Phys.* **18**, 301 (2022).
- [29] C. Mielke, D. Das, J.-X. Yin, H. Liu, R. Gupta, Y.-X. Jiang, M. Medarde, X. Wu, H. C. Lei, J. Chang, P. Dai, Q. Si, H. Miao, R. Thomale, T. Neupert, Y. Shi, R. Khasanov, M. Z. Hasan, H. Luetkens, and Z. Guguchia, Time-reversal symmetry-breaking charge order in a kagome superconductor, *Nature (London)* **602**, 245 (2022).

- [30] A. T. Rømer, S. Bhattacharyya, R. Valentí, M. H. Christensen, and B. M. Andersen, Superconductivity from repulsive interactions on the kagome lattice, *Phys. Rev. B* **106**, 174514 (2022).
- [31] Y. Wang, T. Wu, Z. Li, K. Jiang, and J. Hu, Structure of the kagome superconductor CsV₃Sb₅ in the charge density wave state, *Phys. Rev. B* **107**, 184106 (2023).
- [32] X. Wu, T. Schwemmer, T. Müller, A. Consiglio, G. Sangiovanni, D. Di Sante, Y. Iqbal, W. Hanke, A. P. Schnyder, M. M. Denner, M. H. Fischer, T. Neupert, and R. Thomale, Nature of unconventional pairing in the kagome superconductors AV₃Sb₅ (A = K, Rb, Cs), *Phys. Rev. Lett.* **127**, 177001 (2021).
- [33] M. Kang, L. Ye, S. Fang, J.-S. You, A. Levitan, M. Han, J. I. Facio, C. Jozwiak, A. Bostwick, E. Rotenberg, M. K. Chan, R. D. McDonald, D. Graf, K. Kaznatcheev, E. Vescovo, D. C. Bell, E. Kaxiras, J. van den Brink, M. Richter, M. Prasad Ghimire, J. G. Checkelsky, and R. Comin, Dirac fermions and flat bands in the ideal kagome metal FeSn, *Nat. Mater.* **19**, 163 (2020).
- [34] H. Li, H. Zhao, Q. Yin, Q. Wang, Z. Ren, S. Sharma, H. Lei, Z. Wang, and I. Zeljkovic, Spin-polarized imaging of the antiferromagnetic structure and field-tunable bound states in kagome magnet FeSn, *Sci. Rep.* **12**, 14525 (2022).
- [35] M. Kang, S. Fang, L. Ye, H. C. Po, J. Denlinger, C. Jozwiak, A. Bostwick, E. Rotenberg, E. Kaxiras, J. G. Checkelsky, and R. Comin, Topological flat bands in frustrated kagome lattice CoSn, *Nat. Commun.* **11**, 4004 (2020).
- [36] P. Park, J. Oh, K. Uhlířová, J. Jackson, A. Deák, L. Szunyogh, K. H. Lee, H. Cho, H.-L. Kim, H. C. Walker, D. Adroja, V. Sechovský, and J.-G. Park, Magnetic excitations in non-collinear antiferromagnetic Weyl semimetal Mn₃Sn, *npj Quantum Mater.* **3**, 63 (2018).
- [37] B. R. Ortiz, L. C. Gomes, J. R. Morey, M. Winiarski, M. Bordelon, J. S. Mangum, I. W. H. Oswald, J. A. Rodriguez-Rivera, J. R. Neilson, S. D. Wilson, E. Ertekin, T. M. McQueen, and E. S. Toberer, New kagome prototype materials: Discovery of KV₃Sb₅, RbV₃Sb₅, and CsV₃Sb₅, *Phys. Rev. Mater.* **3**, 094407 (2019).
- [38] S.-S. Gong, W. Zhu, L. Balents, and D. N. Sheng, Global phase diagram of competing ordered and quantum spin-liquid phases on the kagome lattice, *Phys. Rev. B* **91**, 075112 (2015).
- [39] J.-X. Yin, S. H. Pan, and M. Zahid Hasan, Probing topological quantum matter with scanning tunnelling microscopy, *Nat. Rev. Phys.* **3**, 249 (2021).
- [40] K. Takasan and M. Sato, Control of magnetic and topological orders with a DC electric field, *Phys. Rev. B* **100**, 060408(R) (2019).
- [41] M. M. Nayga and M. Vojta, Strain tuning of highly frustrated magnets: Order and disorder in the distorted kagome Heisenberg antiferromagnet, *Phys. Rev. B* **105**, 094426 (2022).
- [42] R.-Y. Sun and Z. Zhu, Metal-insulator transition and intermediate phases in the kagome lattice Hubbard model, *Phys. Rev. B* **104**, L121118 (2021).
- [43] M. Fishman, S. R. White, and E. M. Stoudenmire, The ITensor software library for tensor network calculations, *SciPost Phys. Codebases*, **4**, 1 (2022).
- [44] M. Fishman, S. R. White, and E. M. Stoudenmire, Codebase release 0.3 for ITensor *SciPost Phys. Codebases* **4**, r0.3 (2022).
- [45] G. He, L. Peis, E. F. Cuddy, Z. Zhao, D. Li, Y. Zhang, R. Stumberger, B. Moritz, H. Yang, H. Gao, T. P. Devereaux, and R. Hackl, Anharmonic strong-coupling effects at the origin of the charge density wave in CsV₃Sb₅, *Nat. Commun.* **15**, 1895 (2024).
- [46] The scaling factor is obtained as follows. With $\zeta_{\max} \equiv \max\{\zeta(\theta)\}$ and $\zeta_{\min} \equiv \min\{\zeta(\theta)\}$, the equivalent minimum (maximum) value of $E_0(\theta)$ for those angles in the FRG curve are E_{\min} (E_{\max}). Then $\zeta \rightarrow (\frac{\zeta - \zeta_{\min}}{\zeta_{\max} - \zeta_{\min}})(E_{\max} - E_{\min}) + E_{\min}$ gives the desired scale for $\zeta(\theta)$ shown in Fig. 3.
- [47] W. Jiang, M. Kang, H. Huang, H. Xu, T. Low, and F. Liu, Topological band evolution between Lieb and kagome lattices, *Phys. Rev. B* **99**, 125131 (2019).